Journal of Quantitative Spectroscopy & Radiative Transfer 188 (2017) 60–70

Contents lists available at ScienceDirect

Journal of Quantitative Spectroscopy & Radiative Transfer

journal homepage: www.elsevier.com/locate/jqsrt

Hygroscopic growth of atmospheric aerosol particles based on lidar, radiosonde, and in situ measurements: Case studies from the Xinzhou field campaign

Min Lv [a], Dong Liu [b], Zhanqing Li [a,c,*], Jietai Mao [d], Yele Sun [e], Zhenzhu Wang [b], Yingjian Wang [b], Chenbo Xie [b]

[a] State Key Laboratory of Earth Surface Processes and Resource Ecology (ESPRE), College of Global Change and Earth System Science, Beijing Normal University, Beijing 100875, China
[b] Key Laboratory of Atmospheric Composition and Optical Radiation, Anhui Institute of Optics and Fine Mechanics, Chinese Academy of Sciences, Anhui 230031, China
[c] Department of Atmospheric and Oceanic Science and Earth System Science Interdisciplinary Center (ESSIC) University of Maryland, College Park, MD, USA
[d] School of Physics, Peking University, Beijing 100871, China
[e] State Key Laboratory of Atmospheric Boundary Layer Physics and Atmospheric Chemistry, Institute of Atmospheric Physics, Chinese Academy of Sciences, Beijing 100029, China

ARTICLE INFO

Article history:
Received 17 October 2015
Received in revised form
29 December 2015
Accepted 31 December 2015
Available online 15 January 2016

Keywords:
Aerosol hygroscopic growth
Lidar
Radiosonde
In situ measurements
Aerosol chemical compositions

ABSTRACT

Lidar, radiosonde, and ground-based in situ nephelometer measurements made during an intensive field campaign carried out from July to September 2014 at the Xinzhou meteorological station were used to determine the aerosol hygroscopic growth effect in a cloud-capped, well-mixed boundary layer. Aerosol hygroscopic properties at 355 and 532 nm were examined for two cases with distinct aerosol layers. Lidar-derived maximum enhancement factors in terms of aerosol backscatter coefficient derived using a relative humidity (*RH*) reference value of 85% were 1.19 at 532 nm and 1.10 at 355 nm for Case I and 2.32 at 532 nm and 1.94 at 355 nm for Case II. To derive the aerosol particle hygroscopic growth factor at specific *RH* values, the Kasten and Hänel models were used. A comparison of the goodness of fit for the two models showed that the Kasten model performed better. The hygroscopic growth curve for $RH > 90\%$ was much steeper than that for *RH* in the range of 85–90%. The slopes of the lidar-derived enhancement factor curve (measured from 85% to 95% *RH*) and the nephelometer-derived enhancement factor curve (measured from 40% to 62% *RH*) in Case I show similar trends, which lends confidence to using lidar measurements for studying aerosol particle hygroscopic growth. Data from a ground aerosol chemical speciation monitor showed that the larger values of aerosol hygroscopic enhancement factor in Case II corresponded to greater mass concentrations of sulfate and nitrate in the atmosphere.

1. Introduction

The importance of atmospheric aerosols in earth's climate has been widely recognized [1,2]. Aerosols affect solar radiation directly by scattering or absorbing solar radiation and indirectly by acting as cloud condensation

* Corresponding author.
E-mail address: zhanqing@umd.edu (Z. Li).

http://dx.doi.org/10.1016/j.jqsrt.2015.12.029
0022-4073/

nuclei (CCN), which is closely related to aerosol hygroscopicity [1,3,4]. Likewise, the swelling of aerosols due to water vapor uptake enhances their ability to scatter solar radiation. In this way, aerosol hygroscopic growth plays an important role in the earth's radiation budget [5–7].

Numerous studies over the past years have investigated the hygroscopic growth effect on aerosol optical and microphysical properties in terms of the hygroscopic growth factor, or $f(RH)$ where RH is the relative humidity. Much of the recent research has been done using data collected from humidified nephelometers [3,8] and humidified tandem differential mobility analyzers (HTDMAs) [9–11]. However, these instruments have their limitations. For example, because of their experimental set-up, humidified nephelometers cannot expose air samples to $RH \geq 85\%$ without risking condensation on their chilled mirrors, which would result in spurious measurements. HTDMAs have the advantage of being able to size-select aerosol particles before exposing them to a controlled humidity environment, but have difficulties in reaching RH above ~90%. It is the RH range of 85–100% that is of more pertinent to the ability of aerosols to act as CCN. Another limitation of these instruments is that they can change aerosol properties in the process of drying air samples and re-humidifying them again to a certain RH level. Aerosol particles can also be lost in the sampling line.

Lidar remote sensing is an alternative way to study aerosol hygroscopicity. One advantage of using lidars is that measurements can be made at ranges close to saturation. Another advantage is that the enhancement in backscatter due to changes in RH is measured under ambient and unperturbed atmospheric conditions. However, because aerosols sampled by a lidar are not controlled in any way, lidar applications for hygroscopic growth studies must be limited to cases where the same type of aerosol exists in at least a portion of a profile and where RH values vary widely. Observed differences in aerosol properties can be then be attributed primarily to water uptake as RH increases. Many studies have focused on using lidars to study aerosol hygroscopicity with promising results. In general, RH profiles are required for the analysis of aerosol hygroscopicity. Most of these studies, though, make many assumptions to obtain RH profiles [8,12] or use quite distant radiosonde measurements that are not collocated with the lidar used [13]. Besides, few studies have examined the association between lidar-derived aerosol hygroscopic properties and in situ aerosol chemical composition obtained using a ground-based aerosol chemical speciation monitor (ACSM).

In this study, a methodology to investigate aerosol hygroscopic growth primarily based on a three-wavelength Mie polarization Raman lidar (TMPRL) is developed and applied to data collected at the Xinzhou meteorological station in China. A description of the field campaign and the instruments used is given in Section 2. Section 3 describes the methodology and Section 4 presents the results. Conclusions are given in Section 5.

2. Field campaign and instrumentation

An intensive field campaign was carried out from July to September 2014 at Xinzhou in Shanxi Province (Fig. 1). The measurement site was situated at the Xinzhou meteorological station (38.39°N, 112.7°E, at an elevation of 870 m above sea level, or ASL), which is located to the west of the city. The land surrounding the site is a mix of agricultural, residential, and industrial. The temperate continental monsoon climate over this area, along with the increase in local emissions of anthropogenic aerosol particles, may have a strong impact on regional air quality and climate.

For a better understanding of the impact of aerosol hygroscopic growth on aerosol scattering properties, a TMPRL was used. The TMPRL, a self-contained, fully automated system designed for continuously measuring aerosol optical properties such as the extinction

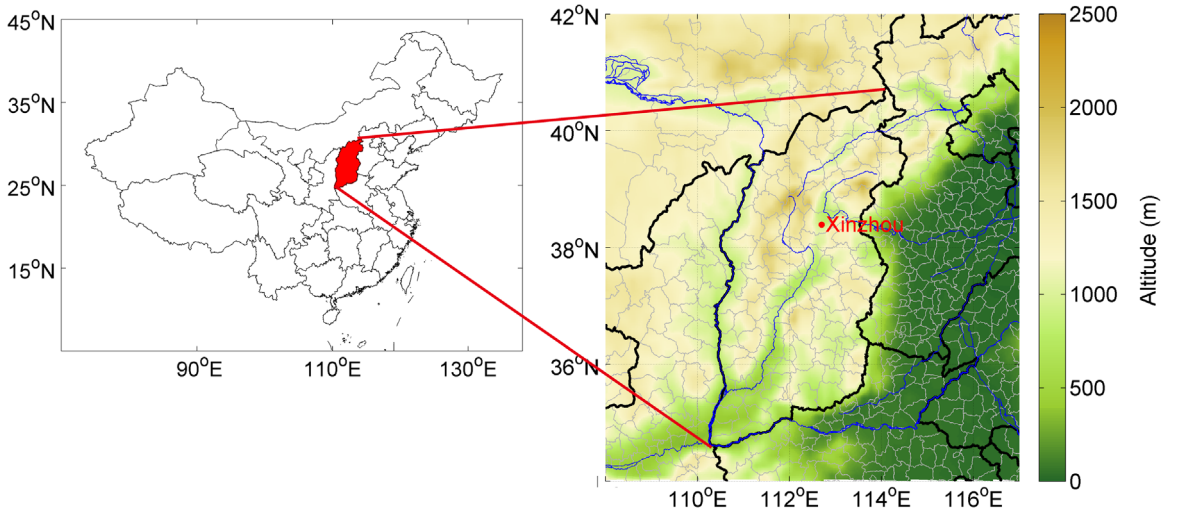

Fig. 1. Left panel: Map showing Shanxi Province in China (red shaded area). Right panel: Location of the experimental site (red solid circle). The altitude is height above sea level. (For interpretation of the references to color in this figure legend, the reader is referred to the web version of this article.)

coefficient, the Ångstrom exponent, and the depolarization ratio, is the primary source of data analyzed in this study [14]. The lidar system emits three laser beams simultaneously at 355, 532, and 1064 nm. The detection system records the elastic signals at these three wavelengths and nitrogen Raman signals at two other wavelengths, namely, 387 and 607 nm. The perpendicular and parallel polarized components of the backscattered signal at 532 nm are also detected, which allows for the study of the depolarization properties of atmospheric aerosols. The TMPRL operates continuously with a time resolution of 30 s and a range resolution of 7.5 m.

Profiles of atmospheric relative humidity (*RH*), temperature and pressure were obtained from radiosonde measurements which is located 50 m north of the TMPRL site. To make sure of the accuracy for these parameters, a comparison experiment between Vaisala radiosonde RS92-SGP and Beidou radiosonde CFL-GNSS-JS was also conducted on 4 September. The comparison results are shown in Fig. 2. It is clearly indicated that both radiosonde systems have almost the same performance. Therefore, the accuracy of the parameters required in our study can be guaranteed with each radiosonde system. Normally, Beidou radiosonde CFL-GNSS-JS was launched four times a day during this field campaign. *RH* profiles were measured at a resolution of 0.1% *RH* and with a total uncertainty of 1.5% *RH*. These measurements are used to derive an extinction-based aerosol hygroscopic enhancement factor, $f(RH)$. Temperature and pressure profiles were also obtained at a resolution of 0.01 °C and 0.1 h Pa, respectively, and with total uncertainties of 0.1 °C and 1 h Pa, respectively, within the atmospheric pressure range of 1080–100 h Pa.

A scattering nephelometer was used to provide another set of $f(RH)$ measurements at ground level. The nephelometer aspirates an air sample, dries it, and then re-exposes it to varying levels of *RH*. *RH* levels in the nephelometer ranged from 40% to 62% in this study. Measurements used here were 15-s averages. Submicron aerosol compositions, including organics, sulfate, nitrate, ammonium, and chloride were also measured at ground level by an aerosol chemical speciation monitor (ACSM) located at the site at a time resolution of ~8 min. A detailed description of the ACSM sampling and data analysis was given in Wang et al. [15].

Back trajectories calculated using the Hybrid Single-Particle Lagrangian Integrated Trajectory (HYSPLIT) model [16] were used to classify the sources of aerosols aloft. Traces of different pollutants have a significant impact on local aerosol hygroscopicity. The back trajectories at different height levels of interest over 36 h were calculated based on 6-hourly archived meteorological data provided by the U.S. National Centers for Environment Prediction's Global Data Assimilation System. The relative errors of the trajectories under low wind conditions are ~40%.

3. Methodology and data processing

3.1. Selection of hygroscopic growth cases

Temporally matched TMPRL and radiosonde profile measurements made under cloud-capped and well-mixed boundary layer conditions form the dataset used to study aerosol hygroscopicity. The lidar range corrected signal at 1064 nm and radiosonde based *RH* profiles [17] were used to select the presence of clouds. Potential temperature (θ) and water vapor mixing ratio (r) profiles were used to determine whether the boundary layer was well-mixed. Firstly, the change rate of potential temperature $\partial\theta/\partial z$ and water vapor mixing ratio $\partial r/\partial z$ among the selected layers are calculated, then we set maximum thresholds as 0.01

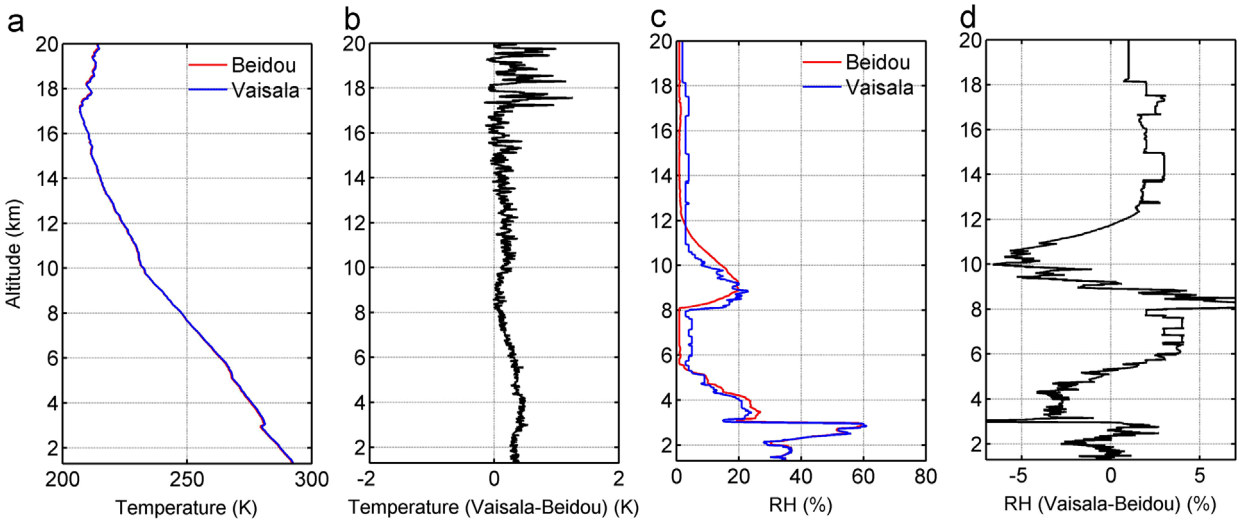

Fig. 2. Vertical profiles of temperature (a) and *RH* (c) from both Vaisala radiosonde RS92-SGP and Beidou radiosonde CFL-GNSS-JS at 00:02 on September 4. Red solid line denotes the Beidou radiosonde and the blue solid line denotes the Vaisala radiosonde. The difference of temperature (b) and *RH* (d) between the profiles detected from the two systems shown in black solid lines. (For interpretation of the references to color in this figure legend, the reader is referred to the web version of this article.)

for the absolute values and 0.005 for the mean values of each variable respectively. Once values among the selected layer are below the threshold range, vertical homogeneity in the analyzed layers can be guaranteed. This information is needed to establish the vertical homogeneity of atmospheric aerosols. In general, constant θ and r profiles are good indicators of well-mixed conditions within the atmosphere [3,8,18]. Aerosol hygroscopic growth is usually happening when enhancement of aerosol optical properties such as the aerosol backscatter coefficient (β) is seen. So layers in the atmosphere where there is an increase in the aerosol particle backscatter coefficient are selected. A coincident increase in *RH* in the layers selected is also required. Once these criteria were met, a more detailed quantitative study of aerosol hygroscopic properties was done. Another ancillary tool called HYSPLIT was also applied in the indication of the atmospheric transport and dispersion of pollutants. Air mass backwards trajectories over 36 h at different altitude levels were calculated using the 6 hourly archived meteorological data provided by the US National Centers for Environmental Prediction (NCEP). Different traces of pollutants have a significant impact on the local aerosol hygroscopicity. All data are reported in Beijing Time (BJT) except for HYSPLIT model output which is reported in Coordinated Universal Time (UTC). Note that BJT=UTC+8 h.

3.2. Aerosol optical properties and hygroscopicity

Profiles of β are derived using the Raman–Mie inversion algorithm at 355 and 532 nm [19,20]. The enhancement factor for the backscattering coefficient, $f_\beta(RH,\lambda)$, is expressed as

$$f_\beta(RH,\lambda)=\beta(RH,\lambda)/\beta(RH_{ref},\lambda), \tag{1}$$

where $\beta(RH,\ \lambda)$ and $\beta(RH_{ref},\ \lambda)$ represent aerosol backscattering coefficients at a certain RH value and at a reference RH value, respectively, at wavelength λ. The lowest value of RH in the aerosol layer under study is chosen as RH_{ref}.

In a similar manner, the effect of water uptake on the nephelometer-measured aerosol total scattering coefficient at 525 nm, $f_\sigma(RH,\lambda)$, is expressed as

$$f_\sigma(RH,\lambda)=\sigma(RH,\lambda)/\sigma(RH_{ref},\lambda), \tag{2}$$

where $\sigma(RH,\lambda)$ and $\sigma(RH_{ref},\lambda)$ represent total scattering coefficients at a certain RH value and at a reference RH value, respectively, at wavelength λ. To derive $f(RH)$ at specific RH values for both the lidar and the nephelometer, the Hänel model and the Kasten model are used. A one-parameter fit, $f_\zeta(RH,\lambda)=\left[(1-RH)/(1-RH_{ref})\right]^{-\gamma}$ [5,21], or a two-parameter fit, $f_\zeta(RH,\lambda)=a\left[1-(RH/100)\right]^{-b}$ [22,23], is selected based upon which model has the best χ^2 goodness of fit. For the Hänel model, γ represents the $f(RH)$ of aerosols. Larger γ values correspond to more hygroscopic aerosol types.

To examine aerosol hygroscopic properties and changes in particle shape, the Ångstrom exponent and the volume linear depolarization ratio were calculated using lidar signals at 355 and 532 nm, and the perpendicular and parallel components of the lidar signal at 532 nm, respectively. If these two parameters simultaneously decrease with altitude in the aerosol layer under study, this indicates that the aerosol particles have become larger and more spherical due to water uptake.

In addition, the total uncertainty of the enhancement factor is very difficult to determine because it highly relies on the uncertainties of many factors including the aerosol properties, the relative humidity, the range of *RH* considered as well as the hygroscopic growth itself and therefore it is not well characterized yet. Future studies are still required to quantify the enhancement factor uncertainty.

3.3. Aerosol chemical properties

Because aerosol acidity is a key parameter affecting aerosol hygroscopic growth, different aerosol chemical compositions may lead to different hygroscopic growth factors [24]. To examine this parameter, the measured NH_4^+ mass concentration is compared with the amount needed to fully neutralize sulfate, nitrate, and chloride ions ($NH_{4\ \mathrm{predicted}}^+$). The predicted mass concentration is given by

$$NH_{4\ \mathrm{predict}}^+=18\times\left(2\times SO_4^{2-}/96+NO_3^-/62+Cl^-/35.5\right), \tag{3}$$

where SO_4^{2-}, NO_3^-, and Cl^- represent the mass concentrations (in $\mu g\ m^{-3}$) of sulfate, nitrate, and chloride ions. The denominators are the molecular weights of these three chemical species and 18 is the molecular weight of NH_4^+. Particles are considered as “more acidic” if the measured NH_4^+ concentration is noticeably (by 25% or more) lower than the predicted value and as “bulk neutralized” if the two values are similar. This approach is valid given that the influences of metal ions, organic acids, and bases on NH_4^+ predicted values are negligible [25].

4. Results and discussions

4.1. Lidar-estimated hygroscopic measurements and trajectories

Two potential cases were selected: one on 29 August 2014 (Case I) and the other on 10 September 2014 (Case II). Radiosonde launch times for each case are 1900 BJT and 1859 BJT, respectively. Data from these cases were first examined to establish that the criteria for proceeding with the analysis of aerosol hygroscopic properties were met.

Fig. 3 shows time series of the lidar range-corrected signal at 1064 nm. Cloud base heights estimated from the radiosonde profile obtained from those particular launches are also shown ($\sim$1575 $\pm$ 6 m for Case I and $\sim$1013 $\pm$ 5 m for Case II). Since the Beidou radiosonde measures data every 1 s with an average ascent rate of about 6 m/s in Case I and 5 m/s in Case II, resulting in a vertical resolution of 6 m (6 m=6 m/s $\times$ 1 s) in Case I and 5 m (5 m=5 m/s $\times$ 1 s) in Case II. A strong increase of the range-corrected signal where a radiosonde-estimated cloud base was identified is seen in both cases. This indicates that a cloud

layer has been reached. Lidar profile data collected close to the times associated with the radiosonde-estimated cloud base measurements are chosen for further analysis.

Potential temperature and water mixing ratio profiles for Case I and Case II are shown in Figs. 4 and 5, respectively. The detailed values of criterion results are listed in Table 1. From this table, it is suggested the analyzed layers are well mixed below the cloud layer.

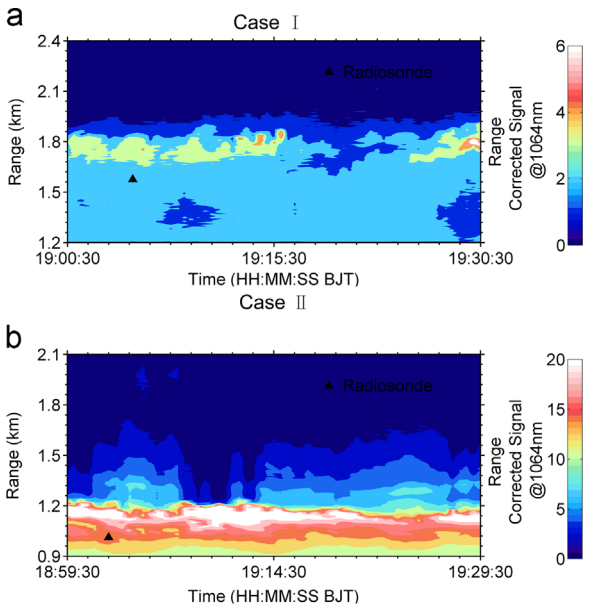

Fig. 3. Time series of the lidar range-corrected signal at 1064 nm for (a) Case I on 29 August 2014 from 19:00:30–19:30:30 BJT and (b) Case II on 10 September 2014 from 18:59:30–19:29:30 BJT. Radiosonde-estimated cloud base heights are shown as black solid triangles in each panel. Note that the limits of the ordinates in (a) and (b) are different.

Figs. 4 and 5 also show vertical profiles of β at 355 and 532 nm for Case I and Case II, respectively. In both cases, there is an increase seen in both β and *RH* between 1440 and 1572 m above ground level (AGL) for Case I (Fig. 4) and between 860 and 1090 m AGL for Case II (Fig. 5). These boundaries define the aerosol layers near cloud layers. Table 2 lists the magnitudes of the aerosol backscatter coefficients at these boundary levels.

Using aerosol backscattering coefficients at 355 and 532 nm, and the RH profiles from Figs. 4 and 5, $f_\beta(RH,\lambda)$ is calculated according to Eq. (1). The reference *RH* value was set to 85%. The aerosol backscattering coefficient increased by a factor of 1.10 at 355 nm and by a factor of 1.19 at 532 nm as *RH* changed from 85% to 93%, i.e., change in backscatter coefficients at 532 nm is stronger than that at 355 nm. Backscattering coefficients obtained at $RH > 98\%$ are not considered here because as RH approaches saturation, a small error in estimating the cloud base height can lead to a large error in RH and subsequently in $f_\beta(RH,\lambda)$ [8]. For Case II (Fig. 6b), the aerosol backscattering coefficient increased by a factor of 1.94 at 355 nm and by a factor of 2.32 at 532 nm as RH changed from 85% to 93%, i.e., change in backscatter coefficients at 532 nm is more than that at 355 nm. In comparison, Wulfmeyer [26] obtained$f_\beta(98\%,\ 532\text{nm})$ of ~2.1 over an island in the Baltic Sea, while Feingold [3] reported $f_\beta(93\%,\ 532\text{nm}) = 1.5$ off the coast of southern California. Given the differences in aerosol types (composition and size), these numbers may not be comparable in a quantitative sense. They are given here just for a broad perspective. The *R*-square values for the two cases in Table 3 show that the Kasten model generally performs better than the Hänel model. The γ values from the Hänel parameterization are larger in Case II than in Case I at both 355 and 532 nm.

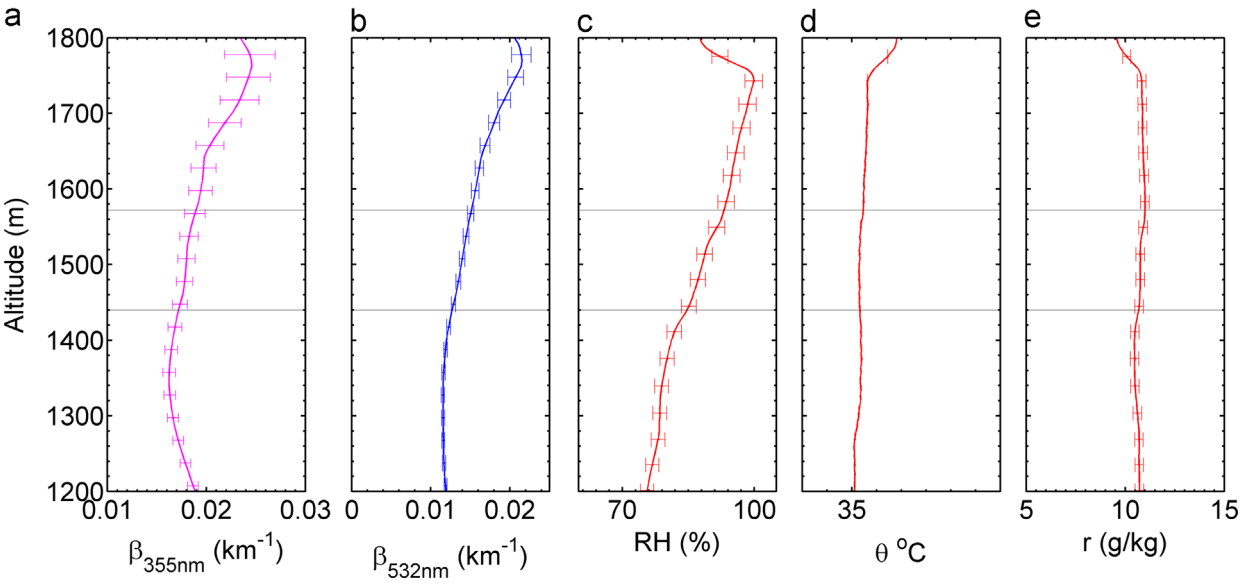

Fig. 4. Vertical profiles of (a) backscattering coefficient at 355 nm, (b) backscattering coefficient at 532 nm, (c) relative humidity, (d) potential temperature, and (e) water mixing ratio. Horizontal gray lines represent the boundaries of the aerosol layer (1440–1572 m above ground level). Data are from 29 August 2014 close to the radiosonde launch time (Case I). Horizontal error bars denote the uncertainty of each property.

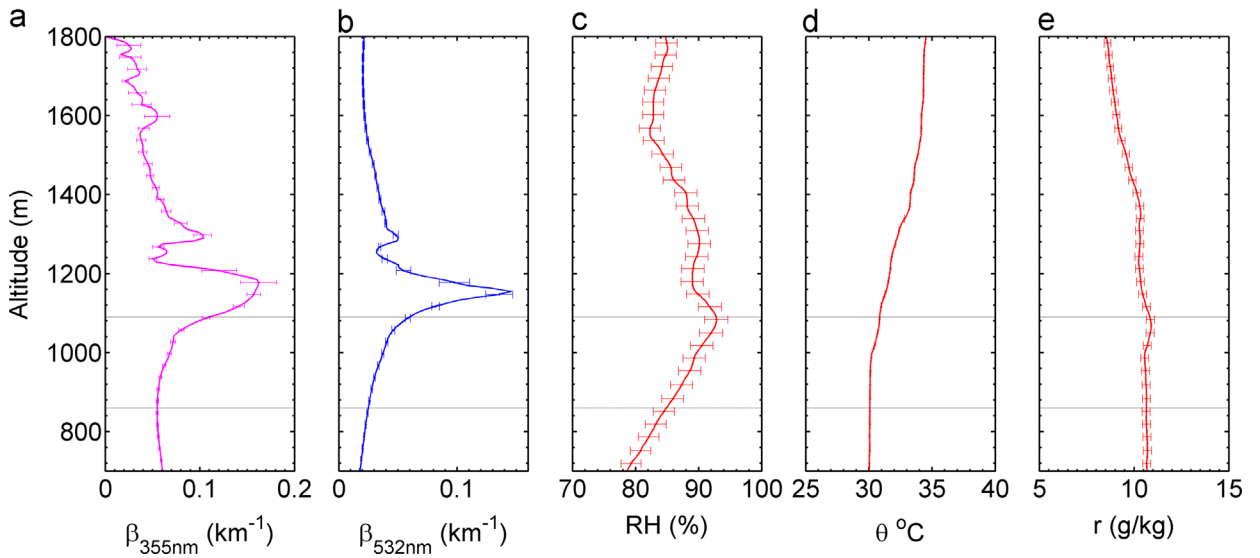

Fig. 5. Same as Fig. 3, but for data from 10 September 2014 close to the radiosonde launch time (Case II). Horizontal gray lines represent the boundaries of the aerosol layer (860–1090 m above ground level). Horizontal error bars denote the uncertainty of each property.

Table 1
Range of values and mean value for $\partial\theta/\partial z$ and $\partial r/\partial z$ among the selected layers in Case I and Case II. θ refers to potential temperature and r refers to water vapor mixing ratio.

	Case I		Case II	
	Range	Mean	Range	Mean
$\partial\theta/\partial z$ (θ Potential temperature)	(−0.0014, 0.0047)	0.0006	(−0.0019, 0.0100)	0.0035
$\partial r/\partial z$ (r Water vapor mixing ratio)	(−0.0021, 0.0074)	0.0023	(−0.0048, 0.0094)	0.0009

A qualitative comparison was made using ground-based nephelometer measurements at 525 nm taken during the period represented by Case I. The trends in the slopes of the lidar-based $f_\beta(RH,\lambda)$ – RH relationship and the nephelometer-based enhancement factor for the light scattering coefficient ($f_\sigma(RH,\lambda)$) – RH relationship are shown in Figs. 6a and 7, respectively. Although nephelometer and lidar remote sensing techniques differ and it is difficult to compare them quantitatively, both profiles show similar increasing trends. This provides confidence in using lidar measurements for studying aerosol hygroscopic growth.

To further validate the optical properties of aerosol hygroscopic growth, the Ångstrom exponent (355–532 nm) and the volume linear depolarization ratio were calculated (Figs. 8 and 9). The two parameters decreased with height in Case I and Case II, which suggests an increase in aerosol particle size at higher altitudes and an increase in particle sphericity. The magnitude of the Ångstrom exponent is close to 0 and sometimes negative, which also suggests the presence of clouds. This is typical of hygroscopic growth. In Case I, the depolarization ratio was less than 0.05 within the aerosol layer (Fig. 8), indicating the dominance of spherical particles in that layer. In Case II, the Ångstrom exponent and the depolarization ratio decreased from 1.114 to 0.499 and from 0.05 to 0.04 (Fig. 9), respectively, within the aerosol layer. The decrease in Ångstrom exponent and the aerosol volume linear depolarization ratio with height in Case II was stronger than in Case I. This may be why $f_\beta(RH,\lambda)$ is higher in Case II. Table 4 summarizes the magnitudes of the Ångstrom exponents and volume depolarization ratios at the boundaries of the aerosol layers representing Case I and Case II.

The aerosol layers present over the Xinzhou site during the two case studies originated from different sources, according to the HYSPLIT-based 36-h back trajectory analysis (Fig. 10). Case I represents an aerosol layer advected in from the desert region of Inner Mongolia (Fig. 10a). This aerosol layer likely contains soil and dust. Case II represents an aerosol layer advected in from a nearby source (Fig. 10b). This aerosol layer is likely comprised of anthropogenic aerosols from south of Hebei Province (38.03°N, 114.26°E). The back trajectory analysis shows that the air mass was traveling close to the ground prior to arrival at the site on 10 September, so likely picked up more and more anthropogenic aerosols along the way.

4.2. Comparison with ACSM measurements

Statistics regarding the mass concentrations of each chemical species at ground level around the time of the Case I and Case II radiosonde launches are shown in Figs. 11a and b. Organics, sulfate, and nitrate were the major aerosol components in both cases. The composition of PM_1 during Case I was 40% organics, 36% sulfate, 13% nitrate, 10% ammonium, and less than 1% chloride. The composition of PM_1 during Case II was 30% organics, 24% sulfate, 32% nitrate, 12% ammonium, and 2% chloride. Fig. 11c shows measured NH_4^+ as a function of predicted NH_4^+. The slope of the linear regression best-fit line is 0.65, which suggests that the particles are more acidic [27]. As a

Table 2
Aerosol backscattering coefficients at 355 and 532 nm at the boundaries (above ground level, AGL) of the aerosol layers representing Case I and Case II. Relative humidity (*RH*) at the boundary levels are given in parentheses.

	Case I		Case II	
AGL (RH)	1440 m (85%)	1572 m (93%)	860 m (85%)	1090 m (93%)
β_{355nm} (km^{-1} sr^{-1})	0.017 ± 0.0015	0.019 ± 0.0005	0.057 ± 0.0002	0.114 ± 0.003
β_{532nm} (km^{-1} sr^{-1})	0.012 ± 0.0005	0.015 ± 0.001	0.025 ± 0.002	0.061 ± 0.003

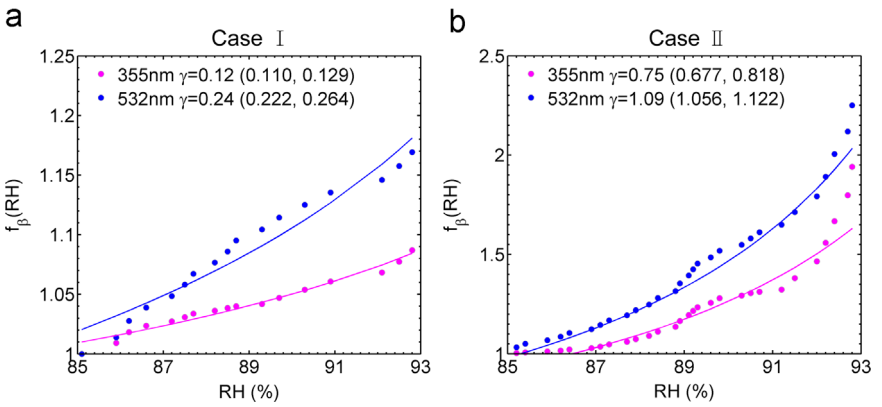

Fig. 6. *f*(*RH*) at 355 nm (magenta dots) and at 532 nm (blue dots) retrieved on (a) 29 August 2014 in the 1440–1572 m aerosol layer (Case I) and (b) 10 September 2014 in the 860–1090 m aerosol layer (Case II). Color-coded best-fit lines are shown. Mean values of hygroscopicity (γ) are also shown. Minimum and maximum values of γ are given in parentheses. The reference *RH* is 85%. (For interpretation of the references to color in this figure legend, the reader is referred to the web version of this article.)

result, sulfate was in the form of NH_4HSO_4 and $(NH_4)_2SO_4$, nitrate was in the form of NH_4NO_3, and the dominant form of chloride was NH_4Cl. NH_4^+ and SO_4^{2-} were correlated with a Pearson's correlation coefficient equal to 0.75 on 29 August (Case I) and 0.71 on 10 September (Case II). This also suggests that the main form of inorganics was NH_4HSO_4 and $(NH_4)_2SO_4$, as well as NH_4NO_3, which does not include NH_4Cl because of its low mass concentration. The hygroscopicity parameter (κ) values for NH_4HSO_4, $(NH_4)_2SO_4$, and NH_4NO_3 are 0.56, 0.5, 0.68, respectively [28,29]. The total mass concentrations of NH_4^+, SO_4^{2-}, and NO_3^- are 68% in Case II, which is greater than that in Case I (59%).

5. Conclusions

A three-wavelength Mie polarization Raman lidar was used to derive aerosol hygroscopic properties in a well-mixed and cloud-capped boundary layer. Data from a Vaisala radiosonde, a ground-based nephelometer, and an ACSM were also collected during the intensive field campaign that took place during the summer of 2014 in Xinzhou, China. Cases where there was a concurrent increase in the aerosol backscattering coefficient and RH were selected to investigate the aerosol hygroscopic growth factor. Additionally, the HYSPLIT model was used to determine the sources and backward trajectories of the air masses arriving at the Xinzhou site during these case studies.

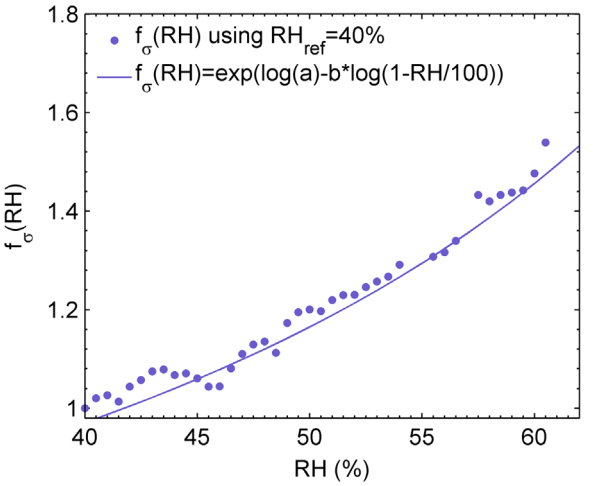

Fig. 7. *f*(*RH*) in terms of nephelometer-measured total scattering coefficient. Data are from 29 August 2014 (Case I). The best-fit line is shown. The reference *RH* is 40%.

Two cases were selected: 29 August (representing a case where pollution was brought in from the northwest, Case I) and 10 September (representing a case where pollution was local, Case II). Maximum values of the aerosol hygroscopic enhancement factor at 355 and 532 nm (*RH*=93%) were 1.10 and 1.19, respectively, for Case I. For Case II, maximum values of the aerosol hygroscopic growth factor at 355 and 532 nm (*RH*=93%) were 1.94 and 2.32, respectively. To derive *f*(*RH*) at

Table 3
The fit parameters and *R*-square goodness of fit for the Hänel model and the Kasten model.

		Case I			Case II		
		γ		*R*-square	γ		*R*-square
Hänel model γ	355 nm	0.12 (0.110, 0.128)		0.90	0.75 (0.677, 0.818)		0.87
	532 nm	0.24 (0.222, 0.264)		0.88	1.09 (1.056, 1.122)		0.98
Kasten model (*a*, *b*)		*a*	*b*		*a*	*b*	
	355 nm	0.8382	0.0979	0.97	0.2058	0.7902	0.92
	532 nm	0.6963	0.2008	0.94	0.1366	1.0389	0.98

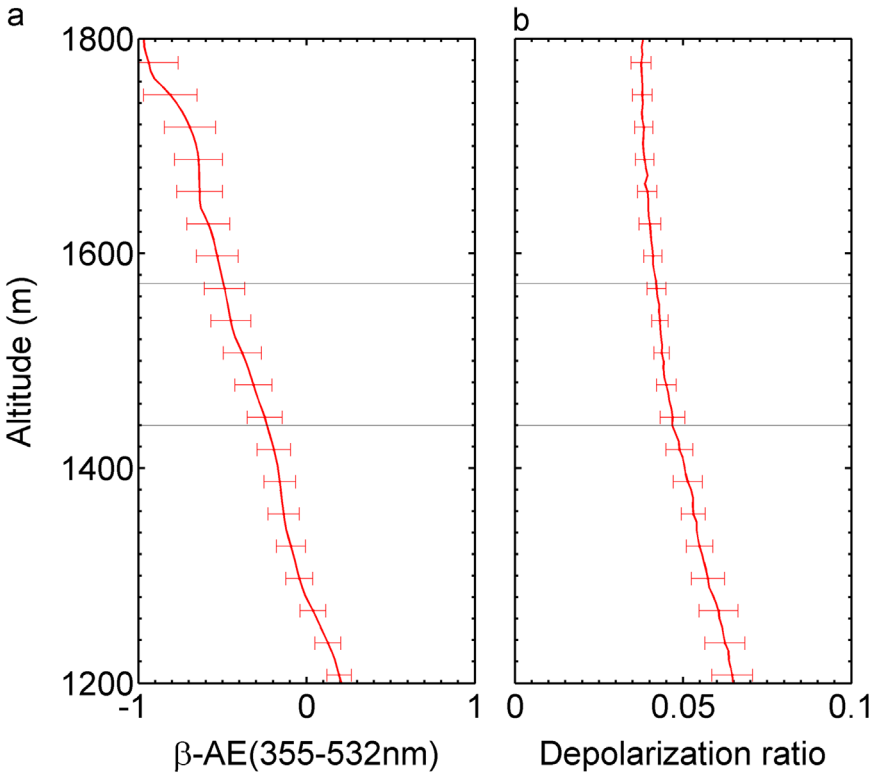

Fig. 8. Vertical profiles of (a) the Ångstrom exponent (355–532 nm) and (b) the depolarization ratio retrieved from lidar data. Horizontal gray lines represent the boundaries of the aerosol layer (1440–1572 m above ground level). Data are from 29 August 2014 (Case II). Horizontal error bars denote the uncertainty of each property.

specific RH values using lidar and nephelometer data, the Hänel model and the Kasten model were used. The values of *R*-square goodness of fit show that the Kasten model performs better than the Hänel model for the two selected cases. Based upon the Hänel parameterization, hygroscopic growth values were larger in Case II than in Case I at both 355 and 532 nm. To explain this difference, in situ measurements from the ACSM were examined. Because aerosol acidity is a key parameter affecting aerosol hygroscopic growth, statistics concerning the mass concentrations of each species comprising the aerosol particles were compiled. Aerosol particles analyzed appear to be acidic, based upon the comparison between measured NH_4^+ and predicted NH_4^+. Aerosol particles from Case II had a greater proportion of hygroscopic components than aerosol particles from Case I. The total mass concentrations of NH_4^+, SO_4^{2-} and NO_3^- are 59% in Case I and 68% in Case II. Using in situ aerosol chemical composition information to explain lidar remote sensing measurements is a way of gaining new insight into aerosol hygroscopic growth.

The simultaneous decrease in the Ångstrom exponent and the volume linear depolarization ratio further confirms the occurrence of aerosol hygroscopic growth. Decreases in both the Ångstrom exponent (355–532 nm) and the volume linear depolarization ratio with altitude in Case II were steeper than in Case I. This is another way of showing the difference in hygroscopicity between the two

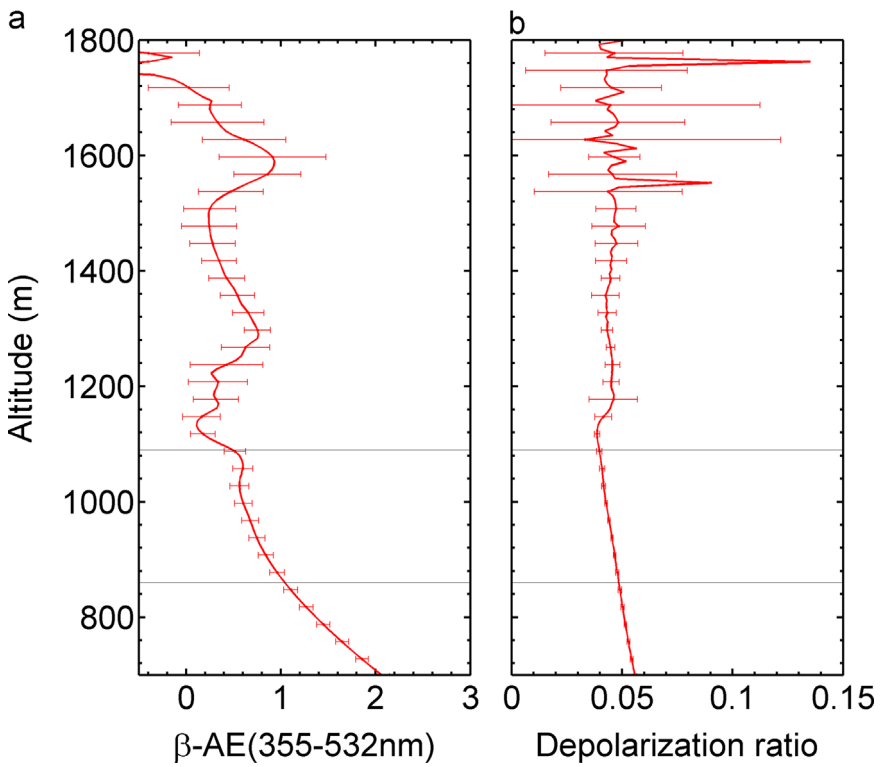

Fig. 9. Same as Fig. 7, but for Case II. Horizontal gray lines represent the boundaries of the aerosol layer (860–1090 m above ground level). Horizontal error bars denote the uncertainty of each property.

Table 4
Ångstrom exponents (355–532 nm) and volume depolarization ratios at the boundaries of the aerosol layers representing Case I and Case II.

	Case I		Case II	
	1440 m	1572 m	860 m	1090 m
β-AE (355–532 nm)	0.1756 ± 0.07	-0.473 ± 0.09	1.114 ± 0.08	0.499 ± 0.13
Depolarization ratio	0.0486 ± 0.003	0.0427 ± 0.002	0.049 ± 0.001	0.040 ± 0.002

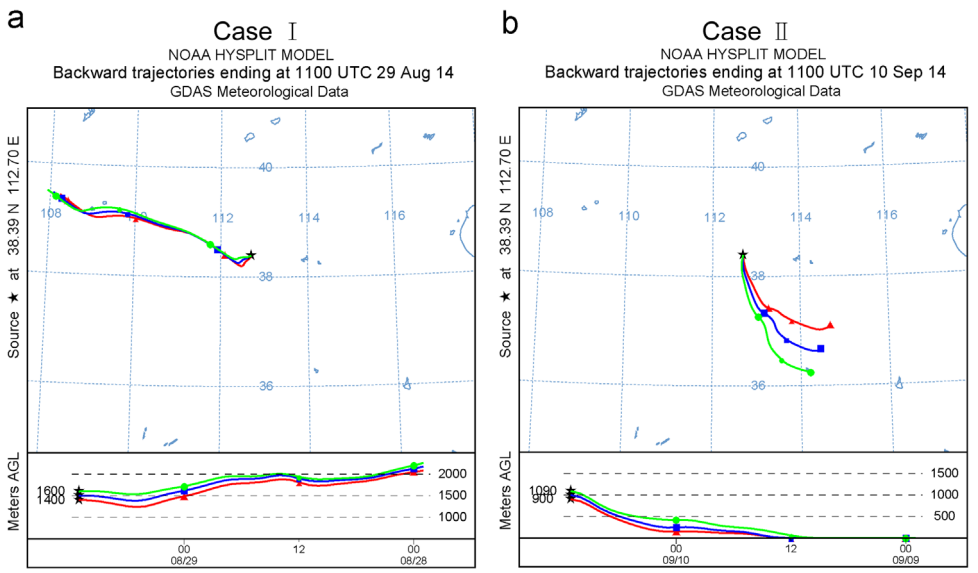

Fig. 10. Thirty-six-hour back trajectories at three height levels ending within (a) the 1440–1572 m layer (Case I) and (b) the 860–1090 m layer (Case II). Trajectories end at the Xinzhou site.

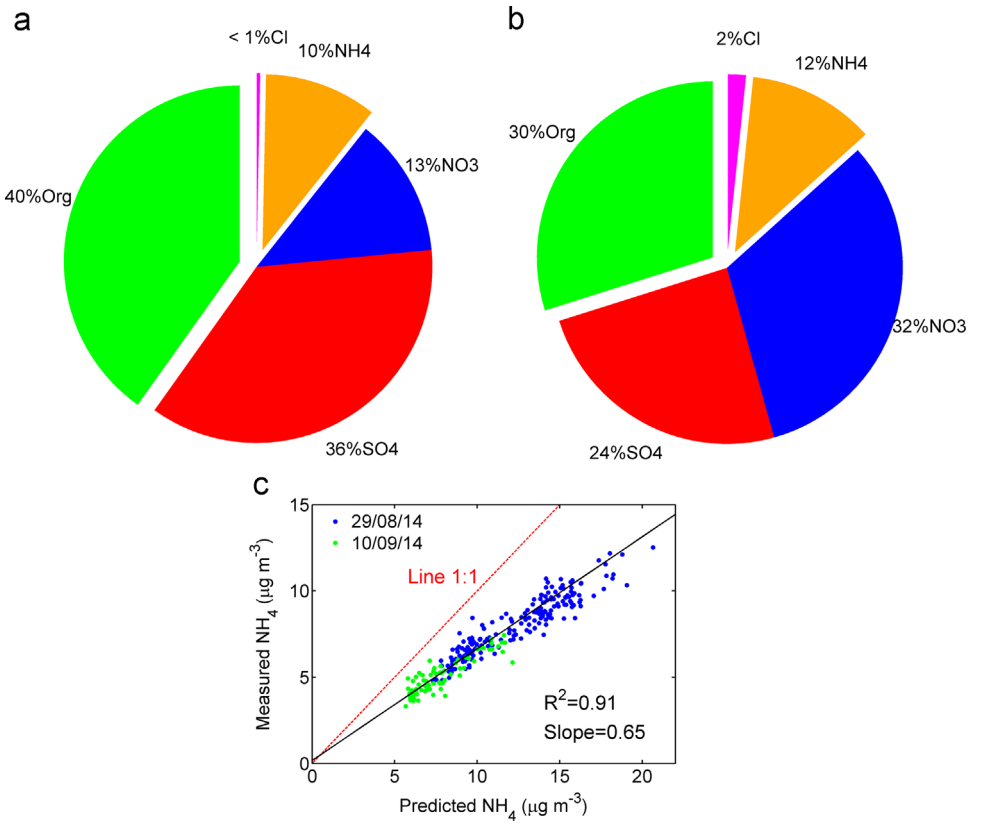

Fig. 11. Submicron aerosol mass fractions (SO_4^{2-}, NO_3^-, NH_4^+, Org, and Cl^-) measured by the ACSM on (a) 29 August 2014 (Case I) and (b) 10 September (Case II). (c) Measured mass concentration of ammonium as a function of predicted mass concentration of ammonium for Case I (blue dots) and Case II (green dots). The predicted mass concentration of ammonium is calculated using Eq. (3). The solid black line is the least squares regression line. (For interpretation of the references to color in this figure legend, the reader is referred to the web version of this article.)

cases considered. However, a cautious interpretation of the Ångstrom exponent is needed given its uncertainty. More detailed analyses of more cases are called for.

This study shows for the first time how in situ aerosol chemical composition measurements can be used to explain aerosol hygroscopic growth. It also shows that the lidar can be a useful tool for measuring aerosol growth, especially if $RH > 85\%$.

Acknowledgments

This work was supported by the National Basic Research Program of China on Global Changes (2013CB955802, 2013CB955804), the National Natural Science Foundation of China (41075016) and US (AGS1118325, AGS1534670), and the ESPRE Project (2015-TDZD-090).

References

[1] Charlson RJ, Schwartz SE, Hales JM, Cess RD, Coakley JJ, Hansen JE, Hofmann DJ. Climate forcing by anthropogenic aerosols. Science 1992;255(5043):423–30. http://dx.doi.org/10.1126/science.255.5043.423.

[2] Vogelmann AM, Flatau PJ, Szczodrak M, Markowicz KM, Minnett PJ. Observations of large aerosol infrared forcing at the surface. Geophys Res Lett 2003;30(12). http://dx.doi.org/10.1029/2002gl016829.

[3] Feingold G, Morley B. Aerosol hygroscopic properties as measured by lidar and comparison with in situ measurements. J Geophys Res 2003;108(D11):4327. http://dx.doi.org/10.1029/2002JD002842.

[4] Padró LT, Tkacik D, Lathem T, Hennigan CJ, Sullivan AP, Weber RJ, Huey LG, Nenes A. Investigation of cloud condensation nuclei properties and droplet growth kinetics of the water-soluble aerosol fraction in Mexico city. J Geophys Res 2010;115(D09204). http://dx.doi.org/10.1029/2009JD013195.

[5] Hänel G. The properties of atmospheric aerosol particles as functions of the relative humidity at thermodynamic equilibrium with the surrounding moist air. Adv Geophys 1976;19(1):73–188.

[6] Hegg DA, Covert DS, Rood MJ, Hobbs PV. Measurements of aerosol optical properties in marine air. J Geophys Res 1996;101(D8):12893–903. http://dx.doi.org/10.1029/96JD00751.

[7] Titos G, Jefferson A, Sheridan PJ, Andrews E, Lyamani H, Alados-Arboledas L, Ogren JA. Aerosol light-scattering enhancement due to water uptake during the TCAP campaign. Atmos Chem Phys 2014;14(13):7031–43. http://dx.doi.org/10.5194/acp-14-7031-2014.

[8] Pahlow M, Feingold G, Jefferson A, Andrews E, Ogren JA, Wang J, Lee YN, Ferrare RA, Turner DD. Comparison between lidar and nephelometer measurements of aerosol hygroscopicity at the southern great plains atmospheric radiation measurement site. J Geophys Res 2006;111(D5):D05S15. http://dx.doi.org/10.1029/2004JD005646.

[9] Brechtel FJ, Kreidenweis SM. Predicting particle critical supersaturation from hygroscopic growth measurements in the humidified TDMA. Part I: theory and sensitivity studies. J Atmos Sci 2000;57(12):1854–71. http://dx.doi.org/10.1175/1520-0469(2000)057<1854:PPCSFH>2.0.CO;2.

[10] Swietlicki E, Hansson HC, Hämeri K, Svenningsson B, Massling A, McFiggans G, McMurry PH, Petäjä T, Tunved P, Gysel M, Topping D, Weingartner E, Baltensperger U, Rissler J, Wiedensohler A, Kulmala

M. Hygroscopic properties of submicrometer atmospheric aerosol particles measured with H-TDMA instruments in various environments—a review. Tellus B 2008;60(3):432–69. http://dx.doi.org/10.1111/j.1600-0889.2008.00350.x.

[11] Zhang F, Li Y, Li Z, Sun L, Li R, Zhao C, Wang P, Sun Y, Liu X, Li J, Li P, Ren G, Fan T. Aerosol hygroscopicity and cloud condensation nuclei activity during the AC3Exp campaign: implications for cloud condensation nuclei parameterization. Atmos Chem Phys 2014;14(24):13423–37. http://dx.doi.org/10.5194/acp-14-13423-2014.

[12] Ferrare RA, Melfi SH, Whiteman DN, Evans KD, Poellot M, Kaufman YJ. Raman lidar measurements of aerosol extinction and backscattering: 2. Derivation of aerosol real refractive index, single-scattering albedo, and humidification factor using Raman lidar and aircraft size distribution measurements. J Geophys Res 1998;103(D16):19673–89. http://dx.doi.org/10.1029/98JD01647.

[13] Veselovskii I, Whiteman DN, Kolgotin A, Andrews E, Korenskii M. Demonstration of aerosol property profiling by multiwavelength lidar under varying relative humidity conditions. J Atmos Ocean Technol 2009;26(8):1543–57. http://dx.doi.org/10.1175/2009JTECHA1254.1.

[14] Tao Z, Liu D, Zhong Z, Shi B, Nie M, Ma X, Zhou J. Measurements of cirrus clouds with a three-wavelength lidar. Chin Opt Lett 2012;10(5):050101. http://dx.doi.org/10.3788/COL201210.050101.

[15] Wang Q, Zhao J, Du W, Godson RA, Wang ZZ, Sun L, Wang Y, Ye X, Zhang F, Li Z, Sun Y. Characterization of Submicron Aerosols at a Suburban Site in Central China; 2015 (in preparation).

[16] Draxler RR, Rolph G. HYSPLIT (HYbrid Single-Particle Lagrangian Integrated Trajectory) model access via NOAA ARL READY website ⟨http://www.arl.noaa.gov/ready/hysplit4.html⟩. NOAA Air Resources Laboratory, Silver Spring, MD; 2003.

[17] Zhang J, Chen H, Li Z, Fan X, Peng L, Yu Y, Cribb M. Analysis of cloud layer structure in Shouxian, China using RS92 radiosonde aided by 95 GHz cloud radar. J Geophys Res 2010;115(D7):D00K30. http://dx.doi.org/10.1029/2010JD014030.

[18] Granados-Muñoz MJ, Navas-Guzmán F, Bravo-Aranda JA, Guerrero-Rascado JL, Lyamani H, Valenzuela A, Titos G, Fernández-Gálvez J, Alados-Arboledas L. Hygroscopic growth of atmospheric aerosol particles based on active remote sensing and radiosounding measurements: selected cases in southeastern Spain. Atmos Meas Technol 2015;8(2):705–18. http://dx.doi.org/10.5194/amt-8-705-2015.

[19] Ansmann A, Riebesell M, Weitkamp C. Measurement of atmospheric aerosol extinction profiles with a Raman lidar. Opt Lett 1990;15(13):746–8. http://dx.doi.org/10.1364/OL.15.000746.

[20] Su J, Liu Z, Wu Y, McCormick MP, Lei L. Retrieval of multi-wavelength aerosol lidar ratio profiles using Raman scattering and Mie backscattering signals. Atmos Environ 2013;79:36–40. http://dx.doi.org/10.1364/AO.49.000108.

[21] Jeong MJ, Li Z, Andrews E, Tsay SC. Effect of aerosol humidification on the column aerosol optical thickness over the atmospheric radiation measurement southern great plains site. J Geophys Res 2007;112(D10202). http://dx.doi.org/10.1029/2006JD007176.

[22] Kasten F. Visibility forecast in the phase of pre-condensation. Tellus 1969;21(5):631–5. http://dx.doi.org/10.1111/j.2153-3490.1969.tb00469.x.

[23] Adam M, Putaud JP, Martins dos Santos S, Dell'Acqua A, Gruening C. Aerosol hygroscopicity at a regional background site (Ispra) in Northern Italy. Atmos Chem Phys 2012;12(13):5703–17. http://dx.doi.org/10.5194/acp-12-5703-2012.

[24] Zhang L, Sun JY, Shen XJ, Zhang YM, Che HC, Ma QL, Zhang YW, Zhang XY, Ogren JA. Observations of relative humidity effects on aerosol light scattering in the Yangtze river delta of China. Atmos Chem Phys Discuss 2015;15(2):2853–904. http://dx.doi.org/10.5194/acpd-15-2853-2015.

[25] Zhang Q, Jimenez JL, Worsnop DR, Canagaratna M. A case study of urban particle acidity and its influence on secondary organic aerosol. Environ Sci Technol 2007;41(9):3213–9. http://dx.doi.org/10.1021/es061812j.

[26] Wulfmeyer V, Feingold G. On the relationship between relative humidity and particle backscattering coefficient in the marine boundary layer determined with differential absorption lidar. J Geophys Res 2000;105(D4):4729–41. http://dx.doi.org/10.1029/1999JD901030.

[27] Zhang Q, Canagaratna MR, Jayne JT, Worsnop DR, Jimenez JL. Time- and size-resolved chemical composition of submicron particles in Pittsburgh: implications for aerosol sources and processes. J Geophys Res 2005;110(D7S09). http://dx.doi.org/10.1029/2004JD004649.

[28] Petters MD, Kreidenweis SM. A single parameter representation of hygroscopic growth and cloud condensation nucleus activity. Atmos Chem Phys 2007;7(8):1961–71. http://dx.doi.org/10.5194/acp-7-1961-2007.

[29] Liu HJ, Zhao CS, Nekat B, Ma N, Wiedensohler A, Pinxteren D, Spindler G, Müller K, Herrmann H. Aerosol hygroscopicity derived from size-segregated chemical composition and its parameterization in the north China plain. Atmos Chem Phys 2014;14(5):2525–39. http://dx.doi.org/10.5194/acp-14-2525-2014.